Scripta Materialia 164 (2019) 52–56

Contents lists available at ScienceDirect

Scripta Materialia

journal homepage: www.elsevier.com/locate/scriptamat

In situ electrochemical dilatometry study of capacity fading in nanoporous Ge-based Na-ion battery anodes

Manni Li [a,b], Zeyu Wang [a,c], Jintao Fu [a], Ke Ma [a], Eric Detsi [a,d,*]

[a] Department of Materials Science & Engineering, University of Pennsylvania, Philadelphia, PA 19104-6272, USA
[b] School of Materials Science, Harbin Institute of Technology, Harbin 150001, China
[c] State Key Laboratory of Advanced Welding and Joining, Harbin Institute of Technology, Harbin 150001, China
[d] Vagelos Institute for Energy Science and Technology (VIEST), Philadelphia, PA 19104, USA

ARTICLE INFO

Article history:
Received 27 December 2018
Received in revised form 20 January 2019
Accepted 21 January 2019
Available online 29 January 2019

Keywords:
Dilatometry
Volume expansion
Nanoporous Ge
Na-ion battery
Capacity fading

ABSTRACT

It is found that crystalline nanoporous Ge can only partially store sodium, with amorphous Na_xGe as the sodiation product. Electrochemical dilatometry techniques were used to measure the corresponding (de)sodiation-induced strains. The capacity and strain amplitude were found to exhibit the same decay trend during long-term cycling, which is expected since the capacity fades because of the volume changes arising during cycling. However, viewed from a different perspective, the similarity between capacity fading and strain decay suggests that one way to mitigate this capacity fading might be by preventing the initial strain from decaying, instead of getting rid of this strain.

The high abundance of raw Na resources has led to extensive research efforts on Na-ion batteries (SIBs) as alternatives to Li-ion batteries (LIBs) for large-scale electrical energy storage applications [1–19]. High-capacity alloy-type sodium compounds such as Na_3P (2596 mAh g^{-1}), $Na_{15}Sn_4$ (847 mAh g^{-1}), Na_3Sb (660 mAh g^{-1}), crystalline NaGe (369 mAh g^{-1}) and amorphous $Na_{1.6}Ge$ (590 mAh g^{-1}) have been proposed as negative electrode materials for SIBs [20–23]. However, phase transformations arising during alloying reaction of Na with P, Sn, Sb and Ge to make the corresponding Na_3P, $Na_{15}Sn_4$, Na_3Sb and Na_xGe ($x = 1$, and 1.6) compounds give rise to large stresses and huge volume changes, resulting in rapid capacity fading [14,24–30]. In the present work, nanoporous Ge was prepared by selective alloy corrosion; the dimensional changes and capacity fading in this material arising during (de)sodiation cycles were investigated in real-time using electrochemical dilatometry techniques. In the following section, we present our experimental methods and procedures.

A Ge-Mn parent material with nominal composition $Ge_{10}Mn_{90}$ at.% was made by melting pure Mn chips (Fisher Scientific, 99.99%) and pure Ge powder (Fisher Scientific, 99.999%) using an electric arc-melter (EQ-SP-MSM207 from MTI). The Ge-Mn binary equilibrium phase diagram predicts the formation of a single face-centered cubic (fcc) phase at the composition of $Ge_{10}Mn_{90}$ (see the yellow highlight in supporting Fig. S1) [31], which is ideal for the fabrication of nanoporous materials by selective alloy corrosion [32,33]. After melting, the Ge-Mn ingot was cut into thin slices with thickness ~0.2 mm for dealloying, during which the sacrificial Mn is selectively removed by free-corrosion in 1 M HCl aqueous solution for 30 min, resulting in nanoporous Ge in the powder form, used to prepare a Ge-based slurry for Na-ion battery electrodes. All the slurry electrode preparation steps were carried out in an argon-filled glovebox (MBraun) with water and oxygen content below 0.1 ppm [34]. During this process, the synthesized nanoporous Ge was further crushed into fine powder, and mixed with conductive additives (carbon black, carbon nanofibers and graphene nanosheets mixture) and with the 40 mg ml^{-1} PVDF/NMP solution used as the binder [23,35]. Details on the slurry preparation and coin cell assembly are added in section 2 in the supporting information. At the end of this process nanoporous Ge-based composite electrodes with 1 cm diameter, for coin cells experiments, and 6 mm diameter, for *in situ* dilatometry, were made onto a 9 μm-thick copper current collector. Specific details on equipment and setup used for morphology and electrochemical characterizations are found in sections 3.1 and 3.2 in the supporting information. The macroscopic dimensional changes in the composite electrode (*i.e.* nanoporous Ge grains embedded in carbon matrix) were measured *in situ* during (de)sodiation cycles using a high-precision electrochemical dilatometer (ECD-3-nano) with ~5 nm resolution [36]. This dilatometer is made of an electrochemical unit for strain measurements referred to as E-Cell (see Fig. S2a), which can be removed from the main setup (see Fig. S2b) and (dis)

* Corresponding author at: Department of Materials Science & Engineering, University of Pennsylvania, Philadelphia, PA 19104-6272, USA.
E-mail address: detsi@seas.upenn.edu (E. Detsi).

https://doi.org/10.1016/j.scriptamat.2019.01.030
1359-6462/

assembled in an argon-filled glovebox. Specific details on strain measurements during *in situ* dilatometry are found in section 3.3 in the supporting information. In the following sections, we present our experimental results and discussion.

Energy-dispersive X-ray spectroscopy (EDX) suggests that the atomic ratio between Ge and Mn changes from ~11:89 before dealloying (Fig. 1a), to ~93:7 after dealloying (Fig. 1b). The very small oxygen signal from the EDX in Fig. 1b suggests that the fabricated nanoporous Ge was not converted into its oxide during dealloying and post-dealloying characterization. The residual carbon signal before and after dealloying comes from the carbon conductive tape substrate used during EDX characterization. Fig. 1c shows the XRD patterns of the Ge-Mn parent material before (red) and after (blue) dealloying. The XRD pattern of the starting $Ge_{10}Mn_{90}$ parent alloy is similar to that of γ-Mn fcc structure with Fm-3m space group from the Materials Project's database (https://materialsproject.org/materials/mp-8634/), which is in agreement with the prediction from the Ge-Mn equilibrium phase diagram (see yellow area in Fig. S1) [31]. After dealloying, the corresponding nanoporous Ge is crystalline with fcc crystal structure (Fd-3m space group, ICCD PDF no. 04–0545), as depicted by the blue XRD pattern in Fig. 1c. Typical scanning electron microscopy (SEM) images of nanoporous Ge are shown at low and high magnifications in Fig. 1d and e, respectively. A porous morphology is observed with a broad ligament size distribution in the range between ~100 and 300 nm. Additional SEM images are included in Fig. S3.

XPS analysis was carried out to study the surface chemical composition of the synthesized nanoporous Ge (see Fig. 2). The following elements were detected from the XPS survey, in agreement with EDX data: Ge, Mn, O and C. The near-surface Ge-to-Mn ratio was found to be ~96:4, which is close to the bulk ratio of ~93:7 obtained from EDX data. GeO_x and MnO_x were detected near the surface of nanoporous Ge as it can be seen from Fig. 2 (see also section 3.4 in the supporting information for specific details). These residual oxides are unavoidable since an aqueous corroding medium was used to prepare these nanoporous Ge. However, the fact that no strong oxygen signal was detected from the EDX of dealloyed nanoporous Ge, suggests that the amount of residual surface oxide is negligible, meaning that the impact of surface oxide on the electrochemical performance of nanoporous Ge should be minimum [23,35].

Prior to strain measurements, the electrochemical performance of the nanoporous Ge composite electrodes was investigated in a coin cell configuration. The SEM images in Fig. S4a and b show the typical cross sections of the nanoporous Ge composite electrode consisting of nanoporous Ge powder embedded in a carbonaceous matrix, made of conductive additives and binder, cast onto on a ~9 μm-thick Cu foil used as current collector. The slurry thickness for strain measurements

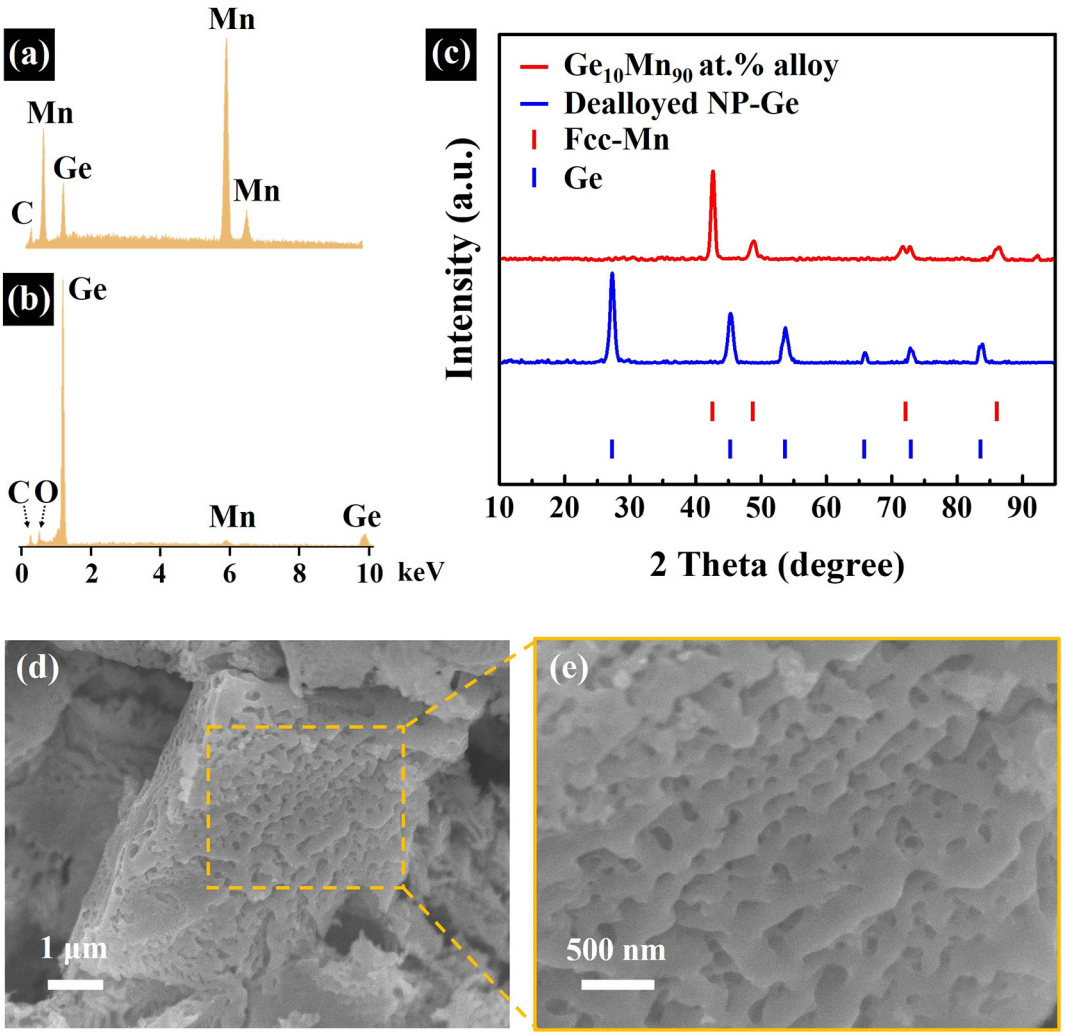

Fig. 1. (a) EDX spectrum of $Ge_{10}Mn_{90}$ at.% before dealloying and (b) corresponding EDX spectrum of nanoporous Ge after dealloying. The strong Mn signal in the parent alloy almost completely disappears after the dealloying process. (c) XRD patterns of the $Ge_{10}Mn_{90}$ at. % parent alloy before dealloying (red pattern) and after dealloying (blue pattern). (d) Low and (e) high magnifications SEM images of nanoporous Ge (additional SEM images can be found in Fig. S3).

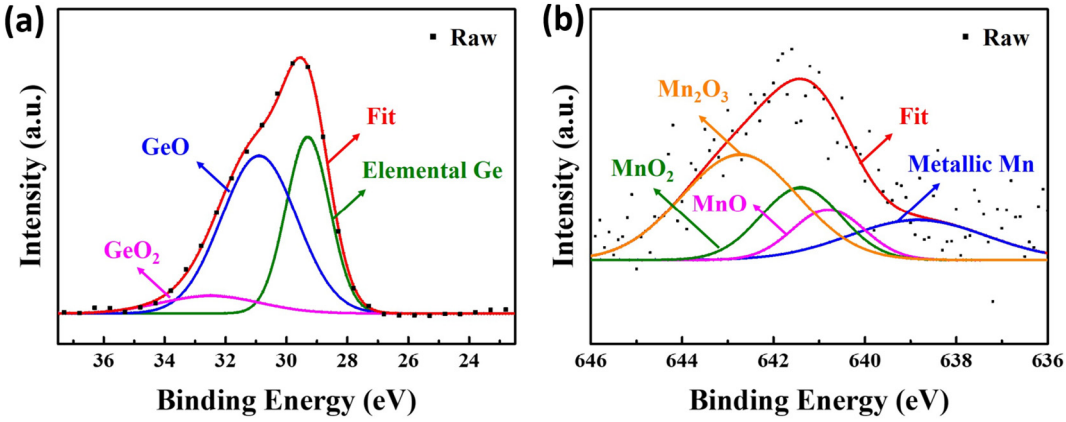

Fig. 2. Analysis of the surface chemical composition of the synthesized nanoporous Ge. Deconvoluted high-resolution (a) Ge 3d and (b) Mn 2p core level spectra, respectively.

was ~25 μm as measured from SEM images (see Fig. S4b). The typical cyclic voltammogram (CV) of the nanoporous Ge composite electrode recorded in the voltage range between 0.02 V and 1.6 V *versus* Na/Na^+, at the scan rate of 0.1 mV s^{-1}, is shown in Fig. 3a (blue curve). For comparison, the CV of a similar electrode, but made without nanoporous Ge, is also shown (black curve in Fig. 3a). These two CVs suggest that most of the capacity of the composite electrode comes from nanoporous Ge. Thus, in the case of nanoporous Ge composite slurry electrode (blue curve in Fig. 3a), the negative current observed in the broad voltage window between ~1 V down to ~0.03 V during the cathodic sweep is associated with the sodiation of Ge to form Na_xGe compound. The positive current (anodic peak around 0.7 V) observed during the anodic scan is associated with desodiation of Na_xGe back to Ge. Fig. 3b displays the (de)sodiation galvanostatic curves of nanoporous Ge for cycles # 1, 2, 5, 10, 30, 50 at the C-rate of C/5. The irreversible capacity during the first sodiation step can be attributed to the formation of solid-electrolyte interphase (SEI) [37–41]. The reversible capacity of the nanoporous Ge composite electrode initially increases from ~217 mAh g^{-1} during the 1st desodiation step to ~260 mAh g^{-1} during the 2nd desodiation, but gradually decreases down to ~128 mAh g^{-1} after 50 cycles. The initial increase in capacity can be rationalized by the exposure of more active surfaces, as a consequence of sodiation-induced materials pulverization in the 1st cycle [23,34,35]. Such materials pulverization will result in gradual capacity fading during subsequent cycles as illustrated in Fig. 3c, which shows the capacity and Coulombic efficiency as a function of the number of cycles. Fig. 3d shows the Nyquist plots recorded during the first three cycles. The semicircle diameter associated

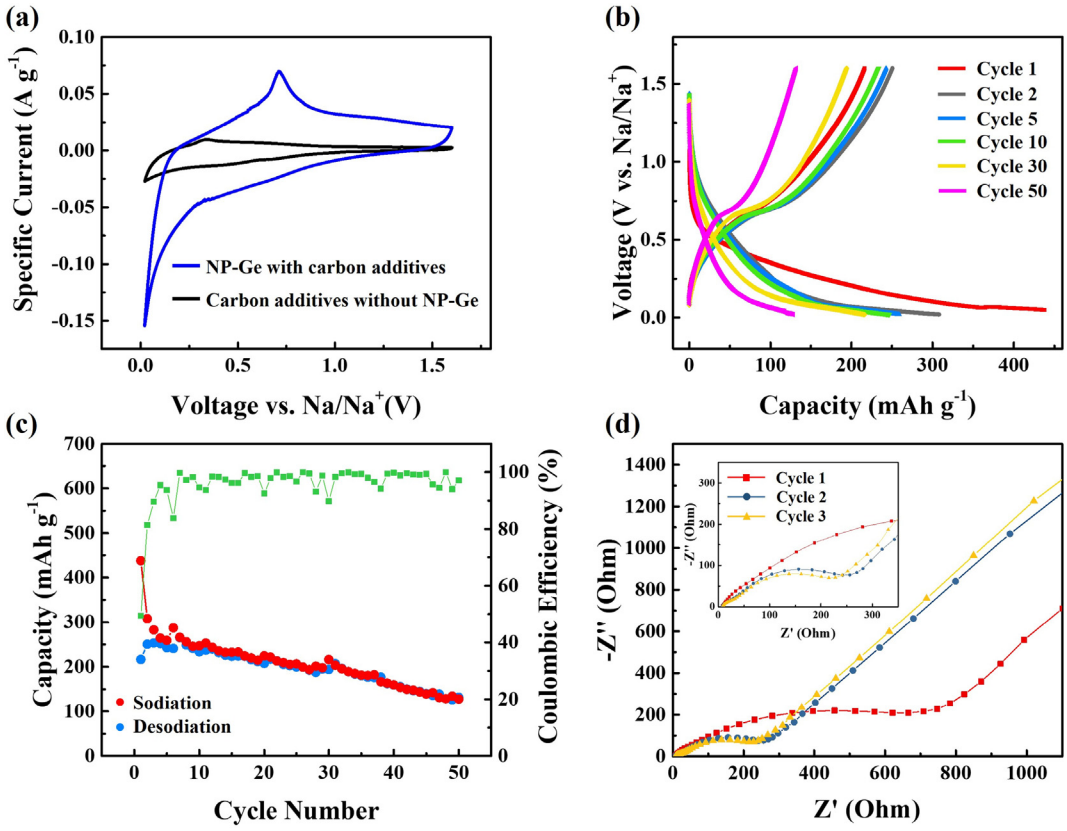

Fig. 3. (a) CVs of nanoporous Ge-based composite electrodes with (blue) and without (black) nanoporous Ge, recorded between 0.02 V and 1.6 V at the scan rate of 0.1 mV s^{-1}. (b) Galvanostatic (de)sodiation curves of nanoporous Ge-based composite electrode at C/5. (c) Corresponding capacity and Coulombic efficiency versus number of cycles at C/5 and (d) Nyquist plots for the first 3 cycles.

with charge transfer resistance significantly decreases from ~800 Ω during the first cycle down to ~270 Ω for the 2nd and 3rd cycles, suggesting that charge transfer during sodiation/desodiation is relatively much easier in the 2nd and 3rd cycles than in the 1st cycle, which is in agreement with surface film (SEI) formation and materials pulverization during the first cycle. The maximum reversible capacity of ~260 mAh g^{-1} achieved in the 2nd cycle in nanoporous Ge is lower than the theoretical capacity of 369 mAh g^{-1} and 590 mAh g^{-1} expected for crystalline NaGe and amorphous $Na_{1.6}Ge$, respectively [22]. Therefore, *ex situ* XRD of (de)sodiated composite electrodes was performed to get more insights into the process (see Fig. S5 in supporting information). The red spectrum in Fig. S5 corresponds to the XRD pattern of as-prepared nanoporous Ge pristine slurry electrode before electrochemical cycling. The green and blue spectra represent the corresponding XRD patterns after the first sodiation, and after the first desodiation, respectively. The intense diffraction peak marked with a black stick pattern at the 2θ value of ~26.5° corresponds to carbonaceous additives in the slurry. This red XRD pattern shows that nanoporous Ge in the pristine slurry exhibits a crystalline structure (see also Fig. 1c). After the first sodiation, the diffraction peaks of Ge remain (red stick pattern Fig. S5), but a broad peak associated with amorphous phase is detected at the 2θ value of ~38° (blue stick pattern Fig. S5). This suggests that the starting crystalline nanoporous Ge is partially converted into an amorphous material (Na_xGe) during the first sodiation. Next, after the first desodiation, the broad peak remains, suggesting that amorphous Na_xGe partially formed during sodiation becomes electrochemically inactive, and cannot be desodiated back to Ge. This is most likely because the huge sodiation-induced volume expansions pulverize the electrode materials, damaging the electrical contacts between the electrochemically active slurry component, the carbon additives and current collectors [37]. As the result, part of the active material becomes electrochemically "dead" during subsequent cycles, which may justify the gradual capacity decay within the first 50 cycles. Materials pulverization may also justify why the starting nanoporous Ge is only partially converted into amorphous Na_xGe during the first sodiation, resulting in the coexistence of both crystalline Ge and amorphous Na_xGe during (de)sodiation, as shown by the green and blue XRD pattern in Fig. S5. In turn, the partial conversion of nanoporous Ge into Na_xGe may justify the low reversible capacity of ~260 mAh g^{-1} achieved in the second cycle in nanoporous Ge, compared to the theoretical capacity of 590 mAh g^{-1} expected for amorphous Na_xGe (x = 1.6) [20]. These sodiation-induced dimensional changes are investigated in the next section.

Electrochemical dilatometry techniques were used to study the macroscopic dimensional changes in the nanoporous Ge composite electrode in real-time during (de)sodiation cycles. Further details on this procedure are found in the experimental section (see Section 3.3 and Fig. S2). Fig. S6a shows the typical raw electrochemical dilatometry data when the change in thickness of the nanoporous Ge composite slurry electrode is measured simultaneously during long-term (de) sodiation cycles up to ~200 cycles (corresponding to ~280 h). The overall strain pattern in Fig. S6a exhibits an irregular deformation wave attributed to sensor drift over time, an unavoidable phenomenon caused by continuous fluctuations in temperature during long-term strain measurements [1,36,42]. Interestingly, nearly reversible strain amplitudes associated with the sodiation/desodiation process are superimposed to the irregular deformation wave, as illustrated by the randomly selected and magnified four areas in Fig. S6-a1, S6-a2, S6-a3 and S6-a4. Two of these selected areas are displayed in Fig. 4a and b below. The average reversible linear strain at the beginning of (de)sodiation process is about 6%, (see Fig. S6-a1), but decreases down to ~0.2% after 50 cycles. It should be emphasized that the carbon-based matrix without nanoporous Ge exhibits a reversible strain below ~0.2%. This suggests that strains above 0.2% measured in our composite electrode come from the dimensional changes in nanoporous Ge. At the start of the process, a reversible strain amplitude of ~6% is recorded in the composite electrode (*i.e.* nanoporous Ge + carbon-based matrix). Since the contribution of the carbon-based matrix to this 6% strain is negligible (<0.2%), it can be concluded that the effective strain in nanoporous Ge is significantly higher than the ~6% strain recorded in the all composite. In general, the overall relative volume expansion $\Delta V/V_0$ for a pure $Na_{1.6}Ge$ phase has been reported to be ~300% [22], corresponding to a linear strain amplitude of ~100%. To further investigate the relationship between the capacity fading and the observed decrease in strain amplitude from ~6% to ~0.2%, both strains

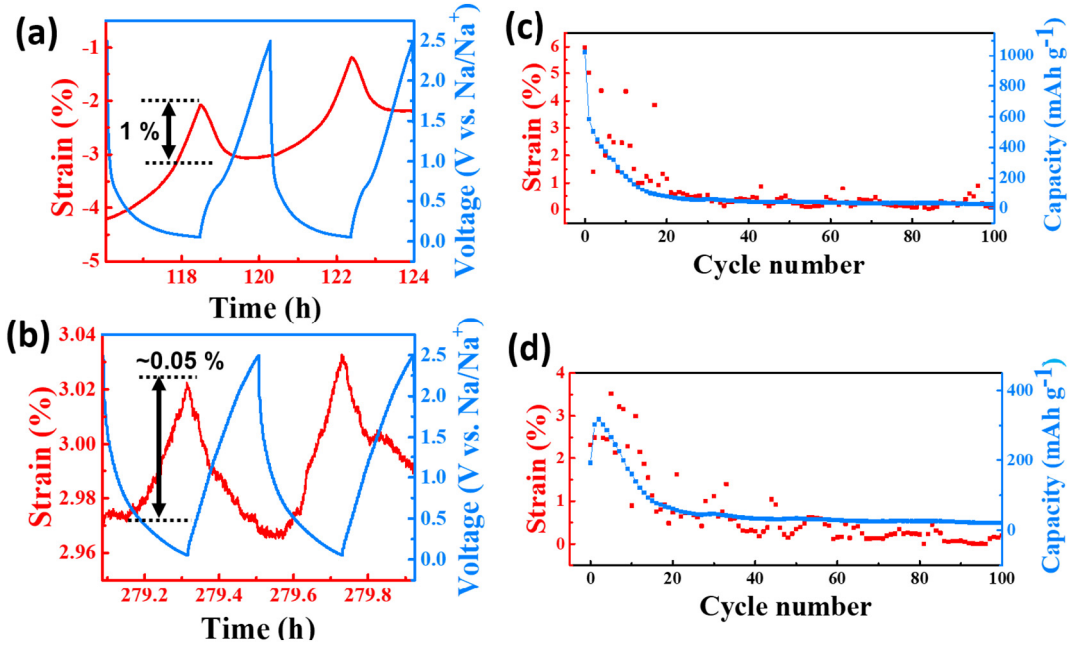

Fig. 4. (a,b) Reversible strains (red) during sodiation-desodiation cycles (blue). The two areas in (a) and (b) are randomly selected from the overall strain data in Fig. S6a. The nearly reversible (de)sodiation-induced strain amplitude decreases from ~6% at the beginning of the process down to ~0.2% after 11.7 days. Trends of the (c) sodiation and (d) desodiation capacities in blue, along with the corresponding strain amplitudes in red, both as a function of the number of cycles.

and capacities were plotted as a function of the number of cycles as illustrated in Fig. 4c and d for the first 100 cycles, where the red data represent the maximum relative expansion and contraction recorded during sodiation and desodiation as a function of the number of cycles, respectively. The blue data in Fig. 4c and d represent the corresponding sodiation and desodiation capacities as a function of the number of cycles, respectively. Both strain amplitudes and capacities decrease in a similar manner during long-term cycling, which is in agreement with the fact that capacity fading is primary caused by the volume expansions in the electrode. In other words, looking from a different perspective, reducing the capacity fading in battery electrodes may require developing electrode materials that will undergo stable reversible volume changes during cycling (*i.e.* the strain amplitude does not decrease during cycling), instead of designing structures that undergo minimum volume expansion as it is currently the case. Since capacity fading and strain decay are proportional, the rate of strain decay should also be proportional to the capacity fading rate. Specifically, for common alloy-type battery electrode materials which exhibit rapid capacity fading at low C-rates, the strain is also expected to rapidly decay at low C-rates.

In summary, nanoporous Ge-based composite electrodes were fabricated and investigated as Na-ion battery anodes. *Ex situ* XRD data of (de)sodiated electrodes suggest that nanoporous Ge does not undergo full sodiation, possibly because of materials pulverization during the first sodiation step. As a consequence, a relatively low reversible capacity of ~260 mAh g^{-1} was achieved after the 2nd desodiation, which represents only ~44% of the theoretical capacity of 590 mAh g^{-1} expected for the $Na_{1.6}Ge$ phase. In subsequent cycles, this reversible capacity gradually decreased from 260 mAh g^{-1} down to ~128 mAh g^{-1} after 50 cycles. This poor cycling stability was further investigated using electrochemical dilatometry techniques, during which the dimensional changes in the electrode were measured *in situ* during (de)sodiation cycles. Linear strain amplitudes of the order of 6% were recorded in the composite electrode at the beginning of the (de)sodiation process. As the electrode was cycled, these strain amplitudes further decayed down to ~0.2% after 50 (de)sodiation cycles. During this long-term cycling, both capacity fading and the decrease in strain amplitudes were found to be proportional, which is expected since the high-capacity in alloy-type battery anodes is directly associated with huge volume changes. View from a different perspective, the similarity between the trends of capacity fading and strain decay suggests that one way to restrict the initial high-capacity from fading might be by preventing the initial reversible strain from decaying, instead of attempting to get rid of these strains as it is currently the case.

Conflicts of interest

There are no conflicts to declare.

Acknowledgements

The authors are thankful to Penn Engineering and NSF for the financial supports through the PI start up and the NSF-EAGER program with Award number: CMMI-1840672. The authors are also thankful to the Vagelos Institute for Energy Science and Technology (VIEST) for the financial support through the 2018 VIEST seed grant. This work was carried out in part at the Singh Center for Nanotechnology, part of the National Nanotechnology Coordinated Infrastructure Program, which is supported by the National Science Foundation grant NNCI-1542153.

Appendix A. Supplementary data

Supplementary data to this article can be found online at https://doi.org/10.1016/j.scriptamat.2019.01.030.

References

[1] B. Rieger, S. Schlueter, S.V. Erhard, J. Schmalz, G. Reinhart, A. Jossen, J. Energy Storage 6 (2016) 213–221.
[2] N. Yabuuchi, K. Kubota, M. Dahbi, S. Komaba, Chem. Rev. 114 (2014) 11636–11682.
[3] L. Zheng, J. Li, M.N. Obrovac, Chem. Mater. 29 (2017) 1623–1631.
[4] J.S. Thorne, R.A. Dunlap, M.N. Obrovac, J. Electrochem. Soc. 160 (2013) A361–A367.
[5] C. Zhu, X. Mu, P.A. van Aken, Y. Yu, J. Maier, Angew. Chem. Int. Ed. 53 (2014) 2152–2156.
[6] Y. Yue, A.J. Binder, B. Guo, Z. Zhang, Z.A. Qiao, C. Tian, S. Dai, Angew. Chem. Int. Ed. 53 (2014) 3134–3137.
[7] Z. Bi, M.P. Paranthaman, P.A. Menchhofer, R.R. Dehoff, C.A. Bridges, M. Chi, B. Guo, X.-G. Sun, S. Dai, J. Power Sources 222 (2013) 461–466.
[8] E. Irisarri, A. Ponrouch, M.R. Palacin, J. Electrochem. Soc. 162 (2015) A2476–A2482.
[9] F. Zhang, Y. Yao, J. Wan, D. Henderson, X. Zhang, L. Hu, ACS Appl. Mater. Interfaces 9 (2017) 391–397.
[10] H. Li, F. Shen, W. Luo, J. Dai, X. Han, Y. Chen, Y. Yao, H. Zhu, K. Fu, E. Hitz, L. Hu, ACS Appl. Mater. Interfaces 8 (2016) 2204–2210.
[11] L. Fu, K. Tang, K. Song, P.A. Van Aken, Y. Yu, J. Maier, Nanoscale 6 (2014) 1384–1389.
[12] X. Han, Y. Liu, Z. Jia, Y.-C. Chen, J. Wan, N. Weadock, K.J. Gaskell, T. Li, L. Hu, Nano Lett. 14 (2014) 139–147.
[13] H. Zhu, Z. Jia, Y. Chen, N. Weadock, J. Wan, O. Vaaland, X. Han, T. Li, L. Hu, Nano Lett. 13 (2013) 3093–3100.
[14] M.D. Slater, D. Kim, E. Lee, C.S. Johnson, Adv. Funct. Mater. 23 (2013) 947–958.
[15] Q. Chen, S. Sun, T. Zhai, M. Yang, X. Zhao, H. Xia, Adv. Energy Mater. 8 (2018) 1800054.
[16] Y. Ma, Q. Guo, M. Yang, Y. Wang, T. Chen, Q. Chen, X. Zhu, Q. Xia, S. Li, H. Xia, Energy Storage Mater. 13 (2018) 134–141.
[17] T. Chen, Y. Ma, Q. Guo, M. Yang, H. Xia, J. Mater. Chem. A 5 (2017) 3179–3185.
[18] C. Chen, Y. Wen, X. Hu, X. Ji, M. Yan, L. Mai, P. Hu, B. Shan, Y. Huang, Nat. Commun. 6 (2015) 6929.
[19] S. Li, Y. Dong, L. Xu, X. Xu, L. He, L. Mai, Adv. Mater. 26 (2014) 3545–3553.
[20] H. Usui, Y. Domi, K. Fujiwara, M. Shimizu, T. Yamamoto, T. Nohira, R. Hagiwara, H. Sakaguchi, ACS Energy Lett. 2 (2017) 1139–1143.
[21] Z. Li, J. Ding, D. Mitlin, Acc. Chem. Res. 48 (2015) 1657–1665.
[22] X. Lu, E.R. Adkins, Y. He, L. Zhong, L. Luo, S.X. Mao, C.M. Wang, B.A. Korgel, Chem. Mater. 28 (2016) 1236–1242.
[23] O. Ruiz, M. Cochrane, M. Li, Y. Yan, K. Ma, J. Fu, Z. Wang, H. Sarah, V.B. Shenoy, E. Detsi, Adv. Energy Mater. (2018) 1–34.
[24] M.R. Palacín, Chem. Soc. Rev. 38 (2009) 2565.
[25] M.M. Thackeray, J.T. Vaughey, C.S. Johnson, A.J. Kropf, R. Benedek, L.M.L. Fransson, K. Edström, J. Power Sources 113 (2003) 124–130.
[26] Y. Zhu, X. Han, Y. Xu, Y. Liu, S. Zheng, K. Xu, L. Hu, C. Wang, ACS Nano 7 (2013) 6378–6386.
[27] S.D. Lacey, J. Wan, A.V.W. Cresce, S.M. Russell, J. Dai, W. Bao, K. Xu, L. Hu, Nano Lett. 15 (2015) 1018–1024.
[28] Z. Dai, U. Mani, H.T. Tan, Q. Yan, Small Methods 1 (2017), 1700098.
[29] L.D. Ellis, B.N. Wilkes, T.D. Hatchard, M.N. Obrovac, J. Electrochem. Soc. 161 (2014) A416–A421.
[30] J. Liu, P. Kopold, C. Wu, P.A. van Aken, J. Maier, Y. Yu, Energy Environ. Sci. 8 (2015) 3531–3538.
[31] A. Berche, J.C. Tedenac, P. Jund, Intermetallics 47 (2014) 23–30.
[32] E. Detsi, Z. Vuković, S. Punzhin, P.M. Bronsveld, P.R. Onck, J.T.M. De Hosson, CrystEngComm 14 (2012) 5402–5406.
[33] J. Fu, Z. Deng, T. Lee, J.S. Corsi, Z. Wang, D. Zhang, E. Detsi, ACS Appl. Energy Mater. 1 (2018) 3198–3205.
[34] H. Yaghoobnejad Asl, J. Fu, H. Kumar, S.S. Welborn, V.B. Shenoy, E. Detsi, Chem. Mater. (2018) https://doi.org/10.1021/acs.chemmater.7b04124.
[35] E. Detsi, X. Petrissans, Y. Yan, J.B. Cook, Z. Deng, Y.-L. Liang, B. Dunn, S.H. Tolbert, Phys. Rev. Mater. 2 (2018), 055404.
[36] K. Ma, J.S. Corsi, J. Fu, E. Detsi, ACS Appl. Nano Mater. C (2018) https://doi.org/10.1021/acsanm.7b00055.
[37] J.B. Cook, E. Detsi, Y. Liu, Y.-L. Liang, H.-S. Kim, X. Petrissans, B. Dunn, S.H. Tolbert, ACS Appl. Mater. Interfaces 9 (2017) 293–303.
[38] H. Kumar, E. Detsi, D.P. Abraham, V.B. Shenoy, Chem. Mater. 28 (2016) 8930–8941.
[39] S. Liu, J. Feng, X. Bian, Y. Qian, J. Liu, H. Xu, Nano Energy 13 (2015) 651–657.
[40] S. Liu, J. Feng, X. Bian, Y. Qian, J. Liu, H. Xu, Nano Energy 13 (2015) 651–657.
[41] J.B. Cook, E. Detsi, Y. Liu, Y.-L. Liang, H.-S. Kim, X. Petrissans, B. Dunn, S.H. Tolbert, ACS Appl. Mater. Interfaces 9 (2017) 293–303.
[42] M. Bauer, M. Wachtler, H. Stöwe, J.V. Persson, M.A. Danzer, J. Power Sources 317 (2016) 93–102.